Permeability–selectivity trade-off for a universal leaky channel inspired by mobula filters

Xinyu Mao[a,1] (ID), Irmgard Bischofberger[a] (ID), and Anette E. Hosoi[a,b,1] (ID)

Affiliations are included on p. 8.

Mobula rays have evolved leaf-shaped filter structures to separate food particles from seawater, which function similarly to industrial cross-flow filters. Unlike cross-flow filtration, where permeability and selectivity are rationally designed following trade-off analyses, the driving forces underlying the evolution of mobula filter geometry have remained elusive. To bridge the principles of cross-flow and mobula filtration, we establish a universal framework for the permeability–selectivity trade-off in a leaky channel inspired by mobula filters, where permeability and selectivity are characterized by the pore-scale leaking rate and the cut-off particle size, respectively. Beyond the classic pore-flow regime in cross-flow filtration, we reveal transition and vortex regimes pertinent to mobula filtration. Combining theory, physical experiments, and simulations, we present distinct features of water permeability and particle selectivity across the three regimes. In particular, we identify an unreported 1/2-scaling law for the leaking rate in the vortex regime. We conclude by demonstrating that mobula filters strike an elegant balance between permeability and selectivity, which enables mobula rays to simultaneously satisfy biological requirements for breathing and filter feeding. By integrating cross-flow and mobula filtration into a universal framework, our findings provide fundamental insights into the physical constraints and evolutionary pressures associated with biological filtration geometries and lay the foundation for developing mobula-inspired filtration in industry.

particle filtration | leaky channel | permeability–selectivity trade-off | mobula ray

To separate particles from their carrying medium, humans have designed numerous filters for air and water purification (1–6), chemical processing (7, 8), food processing (9), electronics fabrication (2), and biomedical applications (10, 11). Various filter designs are generally categorized into dead-end and cross-flow modes (12), with the latter featuring feed flow moving tangentially to the filter surface. Compared to dead-end filters, cross-flow filters are less prone to concentration polarization and fouling due to the high shear rate on the filter surface (12), which leads to longer lifespans and lower energy costs (2).

Echoing industrial filtration, particle filtration is ubiquitous in nature. From immense creatures like baleen whales (13) and whale sharks (14) to tiny organisms such as salps (15) and choanoflagellates (16), filter feeders have evolved diverse filter structures (17–19). These filters function in the aquatic environment (20, 21), in the air (22), or at the air–water interface (23). Apart from feeding, natural filters serve a multitude of functions including sensing (24, 25), water harvesting (26), and purification (27). Despite the considerable differences in their structure, location, and function, many natural filters—like their industrial counterparts—operate in either the dead-end or the cross-flow mode (19, 28, 29). One striking example is the filtering apparatus of mobula rays, a genus comprising two species of manta rays and eight species of devil rays (30). The filter of a mobula ray consists of arrays of leaf-shaped filter lobes (31–33), which facilitate the separation of food particles as water flows tangentially to the filter surface (Fig. 1*A* and *SI Appendix*, Fig. S1). While one may categorize mobula filtration as cross-flow filtration, previous studies suggest the term "ricochet separation" may be more descriptive as particles are observed to bounce off the top of the filters (34). This unique mechanism not only prevents clogging but also enables the separation of particles much smaller than the pores (34).

The resemblance in the working modes invites a comparison between cross-flow and mobula filters. To rationally design cross-flow filters, a pore-flow model, grounded in Poiseuille's (2, 35–37) and Darcy's laws (38, 39), is commonly used to quantify pressure-driven flows through porous membranes. In combination with a steric rejection model, the pore-flow model enables theoretical investigations into the trade-offs between

Significance

Filtration is essential for healthy modern living and for many industrial processes. In filter design, permeability and selectivity are both desirable and are selected following trade-off analyses. The filtering apparatus of mobula rays resembles industrial cross-flow filters but operates in a different parameter regime. To bridge industrial cross-flow and mobula filtration, we establish a universal framework for the permeability–selectivity trade-off in a leaky channel. This universal framework reveals three regimes each of which exhibits distinct laws governing this trade-off. Using our framework, we demonstrate that the geometry of mobula filters has evolved to strike an elegant balance to accommodate breathing and feeding, and derive design principles, which extend beyond traditional filtration regimes, to guide the creation of mobula-inspired filtration devices.

[1]To whom correspondence may be addressed. Email: maoxy@mit.edu or peko@mit.edu.
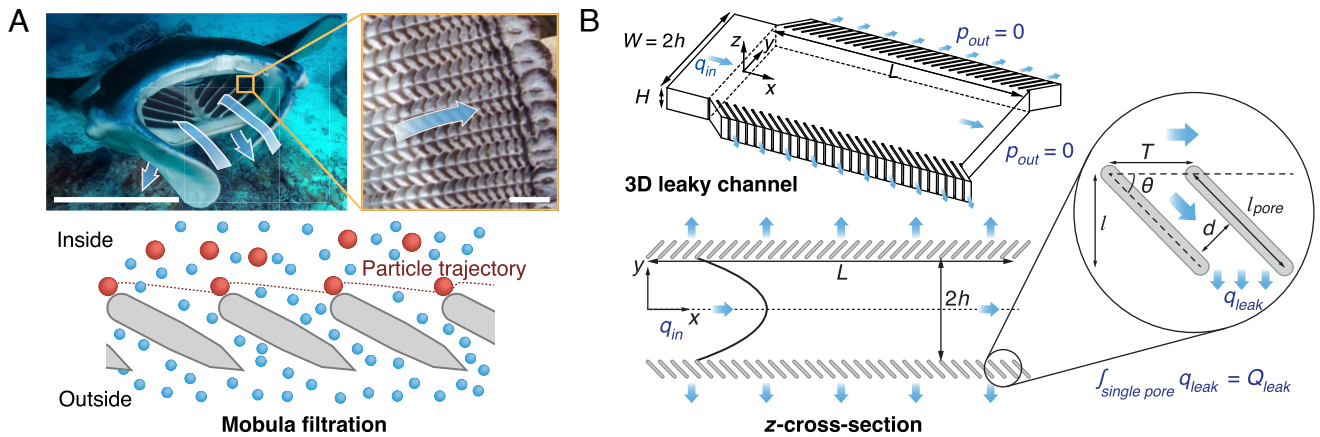
Fig. 1. Universal leaky-channel model bridging mobula filtration and cross-flow filtration. (A) The filtering apparatus of a mobula ray consists of arrays of filter lobes that separate food particles from seawater. The scale bars represent 35 cm (*Left*) and 1 cm (*Right*). (B) Schematic for our universal leaky-channel model. Two arrays of filter plates are symmetric and separated by a distance $2h$, where L denotes the channel length, H the channel height, T the period, d the pore width, l_{pore} the pore length, and θ the tilting angle of the filter plates. The nominal thickness of the filter is $l = l_{pore} \sin\theta$. Fully developed water flow enters the channel with an average velocity q_{in} and leaves the channel through the main outlet and the pores at zero pressure. The average y-velocity component leaking through a period of the filter is denoted as q_{leak}, and the pore-scale leaking rate is $Q_{leak} = q_{leak}TH$. Photo credits for (A): Hubert Yann/Alamy.com [mobula ray (*M. alfredi*)] and Haque *et al.* (mobula filter lobes). The mobula filtration schematic is adapted from ref. 34, and the filter lobe image is adapted with permission from ref. 45 [Copyright (2020) John Wiley & Sons].

permeability and selectivity of porous membranes (37, 40, 41). Such trade-off analyses offer an effective strategy for evaluating the performance of cross-flow filters (35, 42). In contrast to industrial cross-flow filters, the evolutionary pressures leading to the particularly geometry of mobula filters remain unclear; in particular, it is not known whether the permeability–selectivity trade-off represents a key factor in mobula filtration strategies. Given their exceptional performance in anticlogging and separating particles much smaller than the pore size (34), one may question the applicability of the theories for cross-flow filtration (38, 43, 44) to mobula filters. Moreover, a universal framework that integrates both cross-flow and mobula filtration has yet to be established, presenting a broader challenge in understanding particle filtration mechanisms.

In this study, we propose a universal model to explore the physical trade-offs in mobula filter structures, focusing on the permeability–selectivity trade-off in a leaky channel that comprises two periodic arrays of filter plates (Fig. 1B). Our geometric model retains the essential features of the classic cross-flow theory (38, 43, 44); additionally, we introduce a tilting angle for the filter plates such that our model mimics the shape of mobula filters to the first order (Fig. 1). We characterize the permeability and selectivity of the filter with a pore-scale leaking rate and a cut-off particle diameter, respectively. By establishing the trade-off between permeability and selectivity for our mobula-inspired leaky channel, we demonstrate that the shape of the mobula ray filter lobes has evolved to achieve an elegant balance between breathing and filter feeding. Combining experiments, theory, and simulations (with channel flow rates spanning at least three orders of magnitude in both simulations and experiments), we not only reproduce the pore-flow regime for the classic theory but also reveal two additional transition and vortex regimes relevant to mobula filtration. Remarkably, the vortex regime features a hitherto unreported scaling law for the pore-scale leaking rate. The appearance of vortices in the transition and vortex regimes echoes earlier findings of vortices in suspension-feeding fishes (20, 34). With the revelation of these two regimes, our study extends the physical understanding of cross-flow filtration, bridging two types of biological and industrial filtration in a universal framework.

Results

Three Flow Regimes. Our two primary objectives are to characterize the flow rate through a pore (permeability) and the cut-off size of filtered particles (selectivity). Permeability will be considered here first. We fabricate a three-dimensional (3D) leaky channel following Fig. 1B (see Fig. 2A; we add a section of nonleaky wall near the outlet to facilitate fabrication). We visualize the flow at the pore entrance via dye experiments for varying average channel velocities q_{in} (see *Materials and Methods* and *SI Appendix*, Fig. S3A for our experimental setup). For filter plates oriented in both the forward and backward directions, we observe three flow structures as q_{in} increases, which are denoted as vortex-free, partial-vortex (in which a vortex begins to develop at the entrance of the pore), and full-vortex states, respectively (Fig. 2 B and C and Movies S1 and S2). These three flow structures correspond to three different relationships between the pore-scale leaking rate Q_{leak} and the channel velocity q_{in} (see experimental results for channel height $H = 3$ mm in Fig. 2D and *SI Appendix*, Fig. S3B), where Q_{leak} is the volumetric flow rate leaking through one pore. For relatively small q_{in} ($q_{in} < 0.08$ m/s), Q_{leak} is proportional to q_{in}; this linear relationship is also observed in the classic theory based on the pore-flow model (38, 43). For an intermediate q_{in} ($0.08 \leqslant q_{in} < 0.7$ m/s), Q_{leak} is almost independent of q_{in}. For relatively large q_{in} ($q_{in} \geqslant 0.7$ m/s), we identify a power-law scaling between Q_{leak} and q_{in} with an exponent of 1/2.

To explore the conditions for these three relationships, we further measure Q_{leak} as a function of q_{in} for channels with varying heights H (Fig. 2D). As H decreases from 3 mm to 0.5 mm, the proportional relationship ends at an increasing q_{in}, whereas the 1/2-scaling relationship consistently appears for q_{in} on the order of 0.7 m/s or greater. Accordingly, the size of the region connecting the linear to the 1/2-scaling almost disappears for a small H ($H = 0.5$ mm). Additionally, although forward-oriented pores correspond to a slightly higher Q_{leak} for $H = 3$ mm and a small q_{in} (Fig. 2D), the orientation of the pores does not significantly influence the Q_{leak}–q_{in} relationships. These observations reveal three flow regimes at the pore scale, which are governed by different physical mechanisms. We will
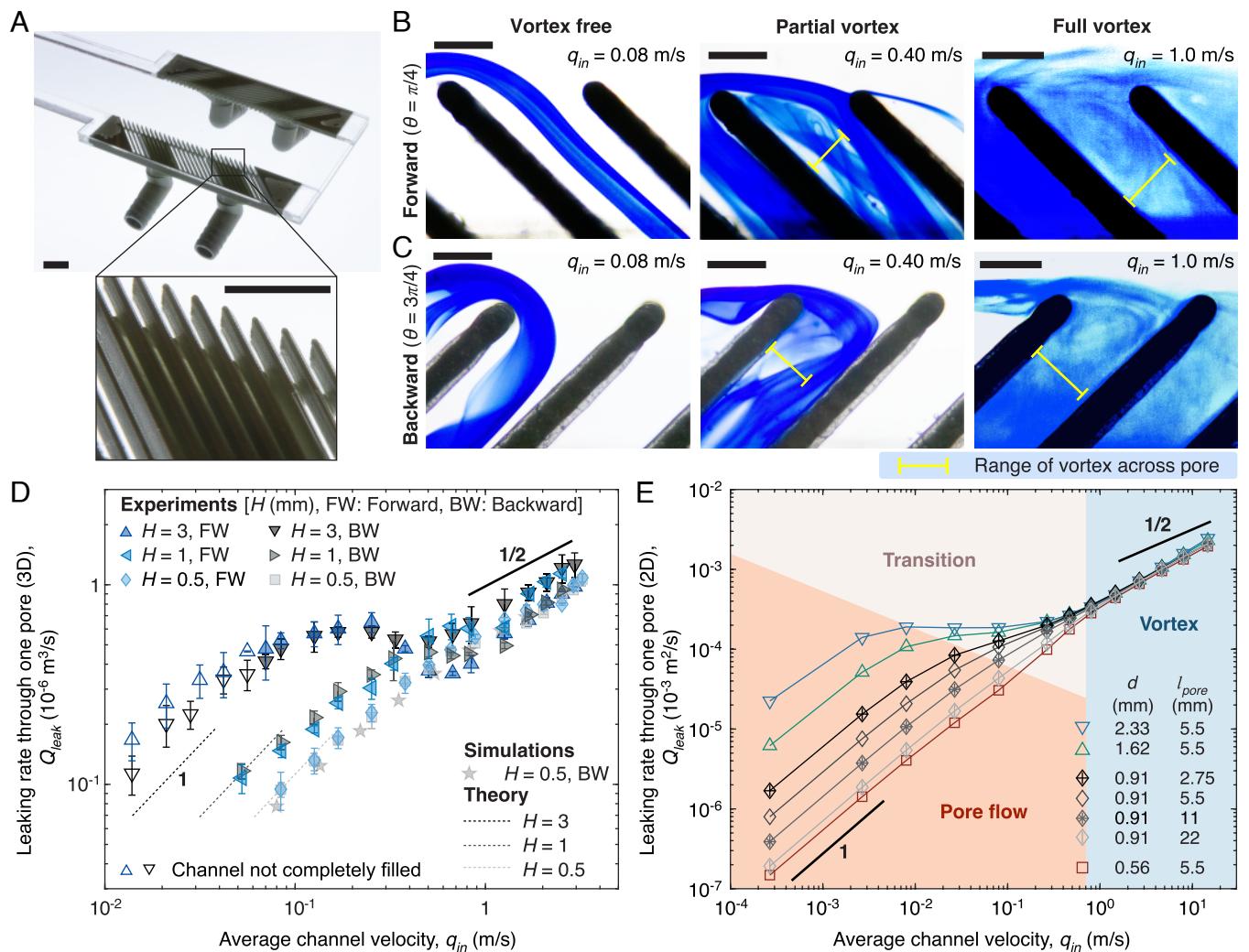
Fig. 2. Pore-scale flow regimes and leaking rates. (*A*) A 3D leaky channel used in our experiments and a close-up view of the pores. (*B* and *C*) Streamlines visualized by dye showing three flow structures at the pore entrance, including vortex-free, partial-vortex, and full-vortex states. The yellow bars indicate the extent to which the vortex blocks the pore entrance. (*D*) Experimentally measured pore-scale leaking rate Q_{leak} versus average channel velocity q_{in} for varying channel heights H and pore orientations, where the forward (FW) and backward (BW) orientations represent the tilting angle $\theta = \pi/4$ and $3\pi/4$, respectively. Experimental results are compared to 3D analytic and numerical results for the same setup. For experiments, the leaking rate Q_{leak} is obtained from the front collector in (*A*), and the unfilled markers denote the runs where the channel is not completely filled with water. (*E*) Numerically computed Q_{leak} versus q_{in} for varying pore widths d and pore lengths l_{pore} in a 2D channel. Three regimes are identified based on the Q_{leak}–q_{in} relationship, including a pore-flow, a transition, and a vortex regime. Scale bars in (*A*) represent 1 cm, and scale bars in (*B*) and (*C*) represent 1 mm.

refer to these three regimes as pore-flow, transition, and vortex regimes.

Pore-Scale Leaking Rate. We first analyze Q_{leak} in the pore-flow regime. Assuming laminar, fully developed flow in the pores, we establish a vortex-free analytic model for 3D leaky channels with a rectangular cross-section (*SI Appendix*, Text A and Fig. S4*A*), which reduces to the classic 2D leaky channel model for $H \to \infty$ (*SI Appendix*, Table S1), where

$$Q_{leak} = q_{in}\lambda h T \frac{\sinh[\lambda(L-x)]}{\cosh(\lambda L)}, \qquad [1]$$

and $\lambda = \sqrt{d^3 \sin\theta/h^3 l T}/2$. Our model also yields a linear relationship between Q_{leak} and q_{in} that agrees with experimental results, especially for channels with height $H = 0.5$ mm and 1 mm (Fig. 2*D*). Our model slightly underestimates Q_{leak} for the channel with $H = 3$ mm. The discrepancy arises from the channel not being completely filled with water in experiments:

our leaky channel is exposed to the air (*Materials and Methods*); due to a high leaking rate relative to q_{in}, the flow is drained before reaching the outlet, exhibiting a contact line pinning at $L^* < L$. We incorporate this phenomenon into our model as a special case (*SI Appendix*, Text A) and obtain a better agreement between experimental data and analytic predictions for $H = 3$ mm (*SI Appendix*, Fig. S4*C*). Additionally, the error bars in the experimentally measured leaking rates may be influenced by the roughness of the 3D-printed filter surface and the fluctuations in the flow rate caused by the centrifugal pump.

We now investigate Q_{leak} in the vortex regime. To provide a simple physical picture, we first consider our 2D numerical results (see *Materials and Methods* and *SI Appendix*, Text B and Fig. S5 for our simulation setup). Note that for both the forward and backward orientations of the pores, our 2D simulations yield Q_{leak}–q_{in} curves with similar shapes as those obtained from 3D experiments, exhibiting three flow regimes (Fig. 2*E* and *SI Appendix*, Fig. S6). Like 3D experiments, our 2D simulations also reveal a 1/2-scaling law between Q_{leak} and q_{in}

in the vortex regime. Moreover, remarkably, all data obtained for varying pore widths d and pore lengths l_{pore} collapse; additionally, Q_{leak} is independent of the tilting angle θ in the vortex regime (*SI Appendix*, Fig. S6B): For laminar flow, the pore-scale leaking rate in the vortex regime does not depend on the details of the pore in our explored parameter space (i.e., $d < l_{pore}$, h and $d \ll L$ in 2D).

To rationalize the 1/2-scaling law and the collapse of the data in 2D, we turn to stagnation-point-flow theory (*SI Appendix*, Fig. S7). In the vortex regime, water leaking from a pore flows through a narrow passage bounded by two separatrices (*SI Appendix*, Fig. S7B), one marking the vortex boundary and the other leading to the stagnation point near the filter tip. The flow near this stagnation point is coupled with the channel flow and the vortex, posing challenges for a full analytic solution; we thus focus on demonstrating its self-similarity (see *SI Appendix*, Text C for detailed derivations). Briefly, we consider the velocity gradient k on a line pointing toward the stagnation point, where k scales linearly with q_{in} (*SI Appendix*, Text D); in the classic stagnation-point-flow theory, k characterizes the flow in the far field. The numerically computed local velocity and pressure are both nondimensionalized using k. In the vicinity of the stagnation point, our dimensionless velocity and pressure align with the classic stagnation-point-flow theory (46) (*SI Appendix*, Fig. S7 C and D), demonstrating the self-similarity of our stagnation-point flow in the vortex regime. Integrating the velocity across the narrow passage gives rise to the scaling $Q_{leak} \propto q_{in}^{1/2}$ (*SI Appendix*, Fig. S7E). Since the narrow passage is confined to a near-wall

region and the stagnation-point flow is dominated by k (or q_{in}), pore-scale geometric parameters including d and l_{pore} do not exert a significant influence on Q_{leak} in the parameter space relevant to Fig. 2E.

In the transition regime, the vortex only partially blocks the pore entrance, and the stagnation-point flow is not strong enough to form a narrow passage for the leakage. Due to the influence of the geometric parameters of the pore, there does not exist a unique scaling for the Q_{leak}–q_{in} relationship.

Delimiting Flow Regimes with Pressure. The three regimes exhibit significant differences in the pressure distribution on the pore scale (Fig. 3 A and B). In the pore-flow regime, we observe a pressure gradient along the pore (see the contour maps for $q_{in} = 2.7 \times 10^{-4}$ m/s). In the vortex regime, however, the high pressure near the stagnation point overshadows the pressure gradient in the pore (see the contour maps for $q_{in} = 1.47$ m/s). Indeed, the vortex stems from a second pressure gradient between the stagnation point and the low-pressure zone behind the filter plate, where the latter arises from the expansion of space at the pore entrance (see the green arrow at the pore entrance indicating the second pressure gradient). Both types of pressure gradients can be identified in the transition regime (see the contour maps for $q_{in} = 0.08$ m/s). Additionally, we present the computed pressure as a function of x/T obtained at a location slightly above the filter tip in *SI Appendix*, Fig. S9, where T is the period. In the pore-flow regime, the pressure decreases along the channel, moderately oscillating around our vortex-free predictions
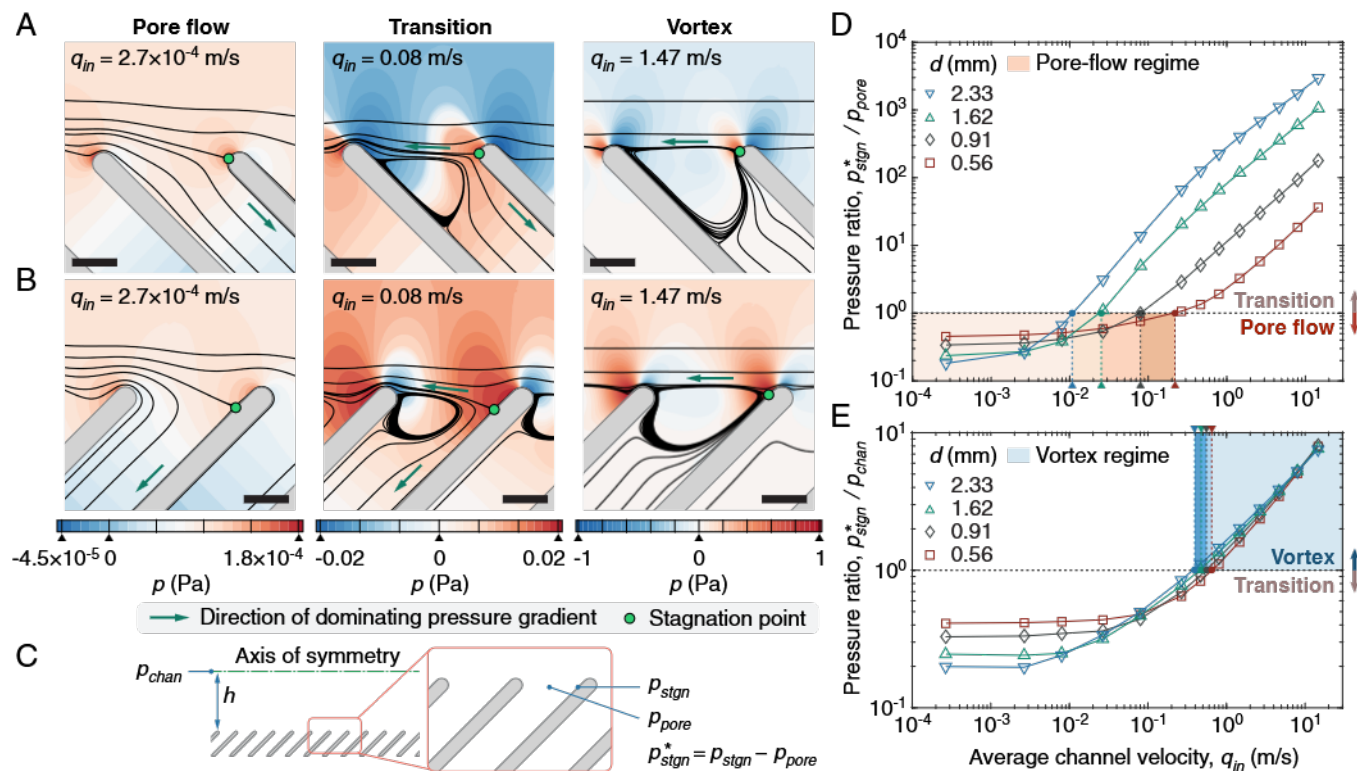
Fig. 3. Delimiting pore-scale flow regimes with pressure. (A and B) Pressure contour maps for a pore oriented in the (A) forward and (B) backward directions for three average channel velocities q_{in}, where $q_{in} = 2.7 \times 10^{-4}$ m/s, 0.08 m/s, and 1.47 m/s correspond to the pore-flow, the transition, and the vortex regimes, respectively. The scale bars in (A) and (B) represent 1 mm. (C) Schematic showing several pressure variables for the delimitation of the three flow regimes. p_{chan} is the analytically calculated pressure at the centerline of the channel based on *SI Appendix*, Eq. **S8**, p_{stgn} is the numerically computed stagnation-point pressure, p_{pore} is the pressure required to drive the computed Q_{leak} through the pore in an otherwise vortex-free scenario, and p_{stgn}^* is the pressure contributed by the stagnation-point flow only. (D) Pressure ratio p_{stgn}^*/p_{pore} as a function of q_{in} for varying pore widths d delimiting the pore-flow and the transition regimes. (E) Pressure ratio p_{stgn}^*/p_{chan} as a function of q_{in} for varying d delimiting the transition and the vortex regimes. The pore length is $l_{pore} = 5.5$ mm for (D) and (E).

[*SI Appendix*, Eq. **S8** in *SI Appendix*, Text A]. By contrast, since the stagnation-point flow becomes dominant in the vortex regime, the pressure above the filter tip fluctuates around a nearly constant level.

The large differences in the characteristic pressure distribution associated with pore and vortex flow enable us to delimit the three pore-scale flow regimes. For this, we introduce several pressure variables (Fig. 3*C*): p_{pore} is a virtual pressure required to drive the computed Q_{leak} through the pore in an otherwise vortex-free scenario. To isolate the contribution from the stagnation-point flow, we denote the elevated pressure relative to p_{pore} at the stagnation point as p_{stgn}^* (see *SI Appendix*, Text D for methods for determining p_{pore} and p_{stgn}^*). Additionally, we denote the analytically calculated pressure at the centerline of the channel as p_{chan}. Comparing these pressures gives rise to the boundaries of the three regimes. As p_{stgn}^*/p_{pore} increases from a small number to $O(1)$, the stagnation-point flow becomes comparable to the Poiseuille flow at the pore scale, which corresponds to a transition from the pore-flow to the transition regime (Fig. 3*D*). When p_{stgn}^*/p_{chan} further increases to $O(1)$, the stagnation-point flow begins to influence the pressure distribution on the channel level, denoting a transition into the vortex regime (Fig. 3*E*). It is important to note that we select 1 as a characteristic pressure ratio for $O(1)$ to delimit flow regimes in Fig. 3 *D* and *E*, yet the transition between flow regimes should be a gradual process.

We end this section by summarizing the velocity and pressure scalings for the three regimes in Table 1 (see proofs in *SI Appendix*, Text D).

Particle Selectivity. We introduce a suspension of polydisperse polystyrene particles (324 ± 51 μm in diameter) into our 3D leaky channel and observe particle trajectories at the pore entrance. Small particles can bypass the vortex and enter the pores, while large particles tend to bounce back to the main channel after colliding with the filter plate (Fig. 4*A*). No clogging occurs at the pore entrance. Additionally, we analyze the size distribution of the particles leaking through the pores under varying q_{in} (Fig. 4*B*). In the pore-flow and the beginning of the transition regimes, the size distribution of the leaked particles is similar to the size distribution before filtration (i.e., the reference distribution). As q_{in} further increases, the average size of the leaked particles decreases significantly in the transition and vortex regimes: the emergence of vortices at the pores accompanies an improvement of the selectivity of the leaky channel.

To rationalize these observations, we explore the cut-off particle diameter $d_{p,c}$ in 2D, which represents the critical particle size that can be filtered by the leaky channel. We estimate $d_{p,c}$ by determining the location of the separatrix above the tip of the previous filter plate (Fig. 4*C*) (47, 48). To illustrate this method, we consider a particle in contact with the filter tip and released at the local fluid velocity. If the particle has a diameter greater than $d_{p,c}$ (see the green particle in Fig. 4*C*), it remains in
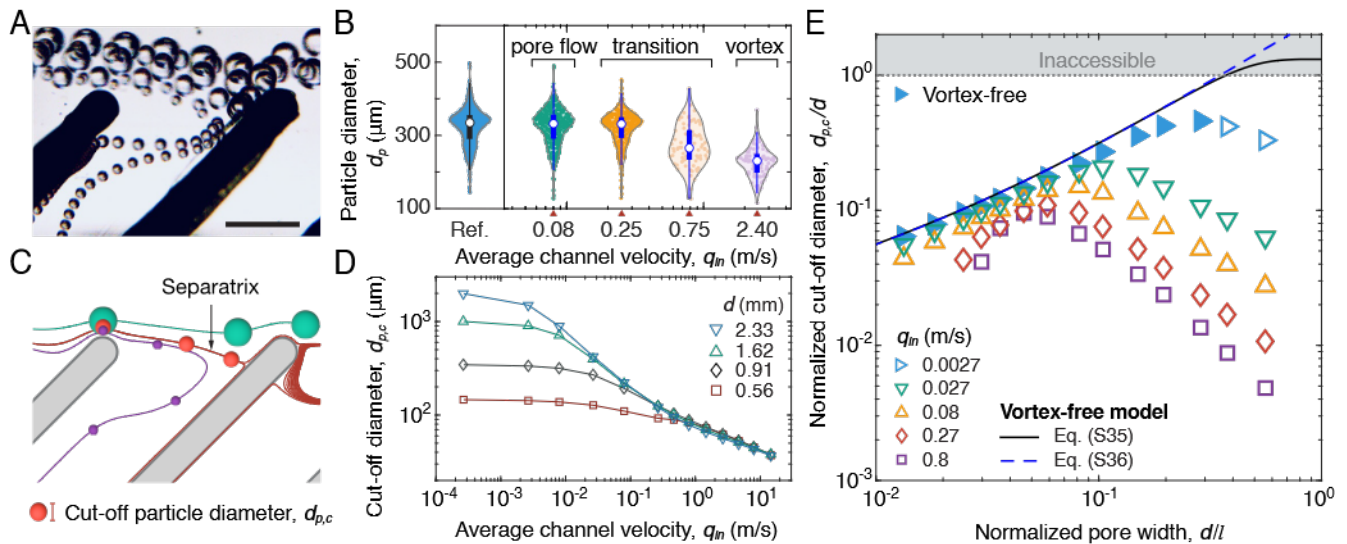
the main channel; otherwise, it leaves the channel through the pore. Based on the pore-scale leaking rate Q_{leak} and the velocity profile across the channel obtained at the filter tip, we propose an implicit function to determine $d_{p,c}$ (see *SI Appendix*, Text E for its functional form and derivations). Further computing $d_{p,c}$ as a function of q_{in} based on 2D simulations, we observe a similar trend to that seen in the 3D experimental results: $d_{p,c}$ is relatively independent of q_{in} in the pore-flow regime and decreases in the transition and vortex regimes (Fig. 4*D*).

The pore width d significantly influences the selectivity of the leaky channel. Holding the pore length l_{pore} and the nominal filter thickness l constant, we numerically investigate the normalized cut-off diameter $d_{p,c}/d$ as a function of the normalized pore width d/l (Fig. 4*E* and *SI Appendix*, Fig. S10). In the limit of very small d/l, the high resistance of the pore gives rise to a small leaking rate and a small $d_{p,c}$. Moderately increasing d/l results in a lower pore resistance and a greater $d_{p,c}/d$. Further increasing d/l up to $O(1)$, the vortex substantially suppresses the fraction of the leakage relative to the channel flow rate, causing $d_{p,c}/d$ to decrease rapidly (Fig. 4*E*; under the laminar assumption). Moreover, in turbulent channel flow, a higher $d_{p,c}/d$ is observed for $d/l \sim O(1)$ compared to that of laminar channel flow (*SI Appendix*, Fig. S10*C*). We explain this difference by comparing the laminar and turbulent velocity profiles across the channel: under the turbulent assumption, a higher shear rate at the pore entrance results in a higher velocity gradient k toward the stagnation point, a higher leaking rate Q_{leak}, and, consequently, a larger cut-off particle size.

Notably, our separatrix method only yields an order-of-magnitude estimate of the actual cut-off particle size. By regarding the particle as a tracer in the fluid, we neglect forces that stem from the nontrivial particle size and inertia (49, 50), e.g., added mass, Basset, lift, and lubrication forces. All of these should certainly be included in a detailed calculation that considers all relevant physical parameters. For example, the lift force in a shape-perturbed leaky channel involves the particle size, the half-channel width, the channel Reynolds number, the leaking rate, the period length, and the shape of the filter plates (51–53). By contrast, the first-order analysis presented herein suffices to reveal the leading factors governing $d_{p,c}$. Compared to the more accurate Lagrangian particle-tracking method, which includes various forces on a particle, the separatrix method provides a simple yet effective strategy for estimating $d_{p,c}$ in 2D: i.e., for a particle released from a filter tip, the separatrix remains close to the computed particle trajectory until it reaches the filter plate (*SI Appendix*, Fig. S11).

It is important to note that our separatrix method does not apply to a 3D channel: since the velocity profile varies significantly for different z-cross-sections, the separatrix likely becomes a curved surface, which gives rise to a range of cut-off particle diameters. With this caveat, the fundamental insights gained from a 2D approximation are applicable to mobula filters.

Permeability–Selectivity Trade-Off. We use mobula filters as a model system to establish the trade-off between permeability and selectivity. Here, permeability and selectivity are characterized by the normalized pore-scale leaking rate $\tilde{Q}_{leak}$ and the cut-off particle diameter $\tilde{d}_{p,c}$, respectively (Fig. 5*A*). As in other types of filters, a small $\tilde{d}_{p,c}$ and a high throughput is desirable for mobula filters (i.e., the upper-left corner of Fig. 5*A*), yet physical laws constrain a simultaneous improvement of permeability and selectivity. Since fully developed laminar, viscous flow and plug (or inviscid) flow represent the two limits of channel flow, we

Table 1. Velocity and pressure scalings in three regimes

Variables	Pore-flow	Transition	Vortex
Velocity gradient, k	$k \propto q_{in}$	$k \propto q_{in}$	$k \propto q_{in}$
Leaking rate, Q_{leak}	$Q_{leak} \propto q_{in}$	—	$Q_{leak} \propto k^{1/2}$
Pressure, p_{pore}	$p_{pore} \propto Q_{leak}$	—	$p_{pore} \propto Q_{leak}$
Pressure, p_{stgn}^*	$p_{stgn}^* \propto k$	—	$p_{stgn}^* \propto k^\chi,$ $\chi \sim 3/2$

Fig. 4. Particle selectivity. (*A*) Particle trajectories experimentally captured in a 3D leaky channel showing different fates of large and small particles, where the channel height is $H = 3$ mm. (*B*) Experimentally measured size distribution of particles leaked from the pores for varying average channel velocities q_{in}, where the reference size distribution is measured for all particles before filtration. Here, the pore width is $d = 0.56$ mm. (*C*) Schematic for the determination of the cut-off particle diameter $d_{p,c}$ based on the location of the separatrix at the tip of the previous filter plate in a 2D channel. (*D*) Numerically computed $d_{p,c}$ as a function of q_{in} for varying pore widths d. (*E*) Numerically computed normalized cut-off particle diameter $d_{p,c}/d$ as a function of the normalized pore width d/l for varying q_{in}, where $l = 15.6$ mm, $l_{pore} = 22$ mm, and the flow is assumed to be 2D laminar. The solid and dashed lines represent the analytic predictions based on our vortex-free model (see *SI Appendix*, Text E for details). The scale bar in (*A*) represents 1 mm.

establish two physical bounds for $(\tilde{Q}_{leak}, d_{p,c})$, which are given by

$$\tilde{Q}_{leak,viscous} = \frac{3}{8}\left(\frac{d_{p,c}}{h}\right)^2 \quad \text{and} \quad \tilde{Q}_{leak,inviscid} = \frac{1}{2}\frac{d_{p,c}}{h} \quad [2]$$

and labeled as "viscous" and "inviscid" in Fig. 5*A*, respectively (see *SI Appendix*, Text F for derivations). For varying pore widths d and channel Reynolds numbers Re_{chan}, our numerically computed $(\tilde{Q}_{leak}, d_{p,c})$ is located within the region between these two bounds. In the laminar regime (e.g., $Re_{chan} = 150$ and $1,350$), the data points are distributed almost parallel to the viscous bound. As Re_{chan} further increases, our results shift toward the inviscid bound. Furthermore, a small d corresponds to small $d_{p,c}$ and $\tilde{Q}_{leak}$.

For mobula rays, feeding and breathing impose additional practical bounds for the accessible $(\tilde{Q}_{leak}, d_{p,c})$ space. Since submillimeter food particles [including small zooplankton, microcrustaceans, ichthyoplankton, and some mesoplankton (34, 54)] are an important food source for mobula rays, we mark the range of 50 to 1,000 µm (34, 54) to denote the size range for submillimeter food particles in Fig. 5*A*. Mobula rays attain insignificant gains for $d_{p,c} < 50$ µm, while most submillimeter food particles leak from the pores for $d_{p,c} > 1,000$ µm. Moreover, all water leaking through the pores passes by the gill tissue before leaving the mobula buccal cavity (*SI Appendix*, Fig. S1). The permeability must thus be above a certain level to guarantee sufficient supply of oxygen. By analyzing the energetics and metabolism of mobula rays (see *SI Appendix*, Text G for derivations), we obtain a lower bound $\tilde{Q}_{leak,min} = 6.1 \times 10^{-5}$, below which mobula rays are likely to experience hypoxia. In combination with the physical bounds, these biological considerations give rise to an accessible region for $(\tilde{Q}_{leak}, d_{p,c})$. We conduct 2D simulations by approximating mobula filter lobes as equivalent filter plates in Fig. 1*B* (see *Materials and Methods* for simulation setup) and find that all ten mobula species (30)

are located within the left part of the accessible region (Fig. 5*A*; see *SI Appendix*, Text G and Table S2 for species data). The data points for the ten mobula species are near the forefront of all our scattered data, toward the desirable—i.e., an optimal balance between permeability and selectivity—upper-left corner of the accessible region. Furthermore, we report the water permeability coefficient and the particle retention rate of the mobula filters, which are two parameters widely used in practical filtration applications (37, 40). The water permeability coefficient of the ten species ranges from 1.1×10^{-4} m s^{-1}Pa^{-1} (*Mobula thurstoni*) to 1.5×10^{-3} m s^{-1}Pa^{-1} (*Mobula hypostoma*), and the retention rate for *Artemia* sp. cysts, a type of micron-sized food particle (34), ranges from 98% to 100% (see *SI Appendix*, Text G and Fig. S12 for details).

Finally, we propose a contour map to illustrate the trade-offs in navigating the design space of mobula-inspired filters (Fig. 5*B*). Based on our vortex-free analytic model, d and l_{pore}/d are chosen as the design parameters. While the analytic model provides first-order estimates of $\tilde{Q}_{leak}$ and $d_{p,c}$, we rely on 2D simulations because our estimated q_{in} for the ten mobula ray species falls within 0.4 to 1.4 m/s (*SI Appendix*, Table S2), a range pertinent to the transition and the vortex regimes. Our numerically computed contour lines for $\tilde{Q}_{leak,min}$ and $d_{p,c,max}$ constitute the left and right biological constraints of the design space, respectively; beyond each boundary, mobula rays suffer from either hypoxia or food deficiency. Additionally, the contour lines for $d_{p,c}$ indicate that the pore width d is more effective in tuning particle selectivity than the pore length l_{pore}. We further analyze the equivalent $(l_{pore}/d, d)$ for mobula filter lobes (see *Materials and Methods* for details) and find that all mobula species fall within the biologically dictated constraints (see the specific location of each mobula species in *SI Appendix*, Fig. S13). The results in Fig. 5 *A* and *B* demonstrate that mobula filters strike an elegant balance between permeability and selectivity, which enables mobula rays to both feed and breathe efficiently.
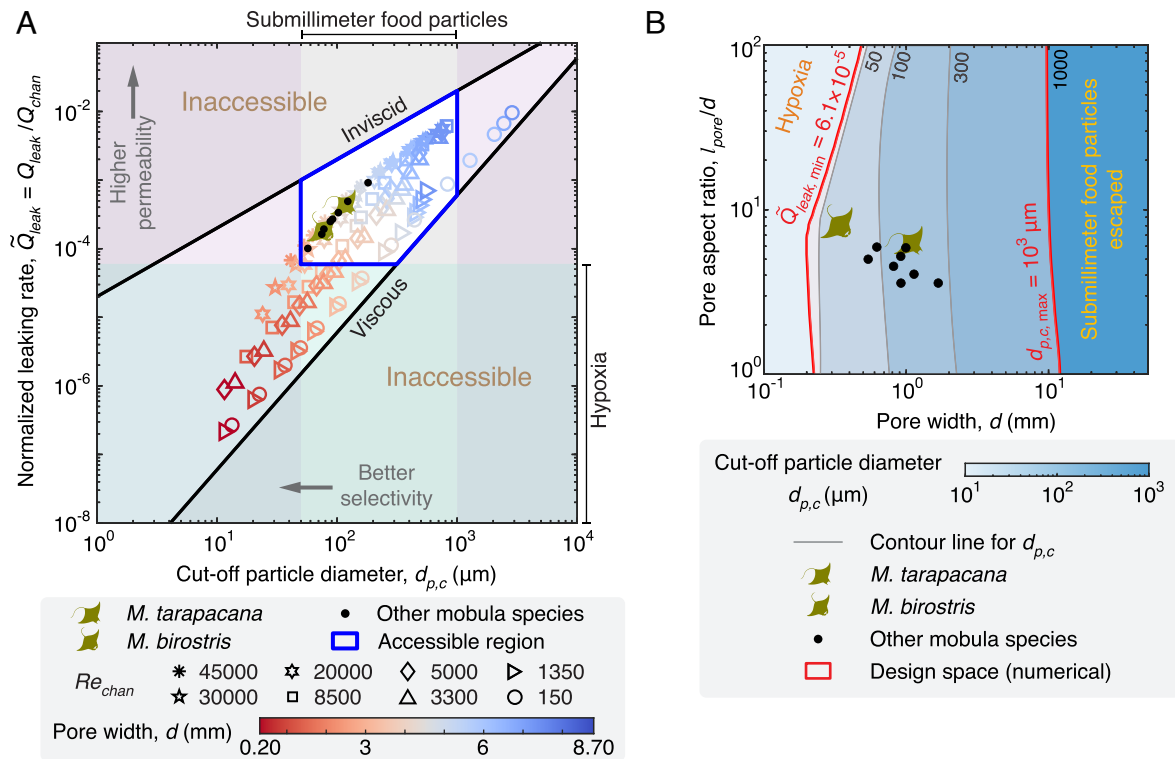
Fig. 5. Mobula filter balances the permeability–selectivity trade-off. (A) Normalized pore-scale leaking rate $\tilde{Q}_{leak}$ versus cut-off particle diameter $d_{p,c}$ for varying pore widths d and channel Reynolds numbers Re_{chan}. Q_{chan} is the channel flow rate. Numerically computed ($\tilde{Q}_{leak}, d_{p,c}$) for ten mobula species are marked in an accessible region determined by the size range of submillimeter food particles, the minimum leaking rate for avoiding hypoxia, and two physical bounds. All scatter data are obtained from 2D simulations. (B) Contour map showing numerically obtained $d_{p,c}$ as a function of the pore width d and the pore aspect ratio l_{pore}/d. Estimated ($l_{pore}/d, d$) for ten mobula species are located in a numerically computed design space determined by the lower bound for $\tilde{Q}_{leak}$ and the upper bound for $d_{p,c}$. The average channel velocity is $q_{in} = 0.6$ m/s for the mobula species in (A) and the numerical contour lines in (B).

It is worth mentioning that $\tilde{Q}_{leak}$ in a mobula ray's cavity may be higher than our conservative lower bound $\tilde{Q}_{leak,min}$ (*SI Appendix*, Text G). Without loss of generality, we consistently base our analyses on two parallel arrays of filter plates throughout this study. In the cavity of mobula rays, however, an angle may exist between the two arrays of filter lobes (*SI Appendix*, Fig. S1), which likely leads to a higher $\tilde{Q}_{leak}$. Apart from the effect of the angle, our 2D model also simplifies some other 3D features of mobula filter lobes (e.g., the leaf-like shapes), which may influence permeability and selectivity. For example, the gaps between two neighboring arrays of filter lobes may result in a higher $\tilde{Q}_{leak}$ (Fig. 1A); in the vortex regime, the leaf-shaped filter lobes can give rise to 3D helical particle trajectories (20), which likely affect the selectivity of mobula filters. Numerically and experimentally resolving flow and particle trajectories on the scale of 3D filter lobes could further improve our understanding of the permeability–selectivity trade-off. Although beyond the scope of this study, the influences of the angle and other 3D features should be addressed in follow-up investigations.

In this study, we focus on the permeability–selectivity trade-off for mobula filters. The principles underlying mobula filters shed light on the design of microparticle filtration devices. Given a desirable water production rate and a target range of particle sizes, one may establish a trade-off diagram and locate an accessible region as in Fig. 5A. An optimal design point within the accessible region can be approached by tuning the pore width and selecting a moderately high channel Reynolds number. Notably, practical applications likely target different particle sizes than

mobula rays. Numerical simulations and the separatrix method are thus desirable to find the most suitable parameter values for the geometric design.

Conclusions

To bridge industrial cross-flow and biological mobula filtration, we have developed a universal framework for the permeability and selectivity in a leaky channel. Our phase diagram comprises pore-flow, transition, and vortex regimes, each featuring distinct characteristics in terms of the pore-scale leaking rate Q_{leak} and the cut-off particle diameter $d_{p,c}$. We find an unreported 1/2-scaling law between Q_{leak} and the average channel velocity q_{in} in the vortex regime. We further propose a diagram that quantifies the permeability–selectivity trade-off for a 2D leaky channel flow. Importantly, mobula filters attain an exquisite balance between permeability and selectivity to fulfill both feeding and breathing functionalities. Since mobula filters are situated in the transition and vortex regimes, their fundamental mechanisms expand the traditional design space of cross-flow filters.

Finally, we emphasize the basic assumptions and limitations of our findings. First, our 1/2-scaling law between Q_{leak} and q_{in} is derived under a laminar flow assumption at the pore scale. For a turbulent channel flow at a very high channel Reynolds number Re_{chan}, however, the coupling between q_{in} and the shape of the channel velocity profile may break down the linearity between the velocity gradient k and q_{in}, which in turn would negate the 1/2-scaling law. Second, we employ the separatrix method to estimate $d_{p,c}$. Despite its success in enabling our trade-off analyses, other

neglected factors, including diffusion, particle inertia, forces acting on particles, and near-wall hydrodynamics, play a role in determining the precise particle trajectory and the cut-off size. Consequently, filter selectivity may be influenced by geometric parameters not revealed by the separatrix method, e.g., the tilting angle θ. Finally, we adopt time-averaged velocity profiles to determine $d_{p,c}$ in 2D turbulent channel flow, yet the random turbulent fluctuations may give rise to a higher $d_{p,c}$ in reality.

Apart from permeability and selectivity, fouling control represents another central question in particle filtration. Future research should investigate the underlying design principles in the context of the observed excellent anticlogging performance of mobula filters (34). By adopting a linear (or "one-link") shape for the filter plates, our study significantly simplifies the structure of mobula filter lobes. Adding complexities to the filter plates (e.g., multilink, multiscale, or 3D structures) and incorporating various forces on particles may give rise to unexpected particle trajectories and unconventional anticlogging properties. Such properties are geometrically induced and do not rely on specific material properties, thus can be applied to diverse filtration applications. We envision that a mobula-inspired framework encompassing permeability, selectivity, and antifouling will substantially expand our physical understanding and design space of particle filtration.

Materials and Methods

Experimental Methods. We employ 3D printing and laser cutting to fabricate the leaky channels. Parallel filter plates and water collectors are printed using a filament 3D printer at a resolution of 50 μm in the z-direction (Prusa i3 MK3S+), and the remaining parts of the channel are prepared by laser cutting acrylic sheets (Universal Laser Systems). The components are then glued together (Weld-On Acrylic Cement). Our channels have an entry length of 50 cm, a half-channel width of 25 mm, a plate thickness of 0.5 mm, and thirty filter plates on each side. The front and rear water collectors correspond to pores 5 to 10 and 20 to 25, respectively. Unless otherwise mentioned, the period length is $T = 3$ mm, and the pore length is $l_{pore} = 5.5$ mm. We circulate deionized water within our experimental apparatus, which consists of the leaky channel, two water tanks, two centrifugal pumps (McMaster-Carr), and one variable-area flow meter (McMaster-Carr) (*SI Appendix*, Fig. S3A). The range of our flow meters spans from 0.02 to 20 gallons per minute.

To visualize the flow at the pore entrance, we inject a 0.71% v/v Brilliant Blue G (Thermo Fisher Scientific) solution from a neighboring pore at a flow rate of 1 mL/min using a syringe pump (Harvard PHD Ultra). The flow is then captured using a digital single-lens reflex camera (Canon EOS7D) equipped with a macro lens (Tamron 28 to 300 mm F/3.5-6.3 XR Di VC). To measure the leaking rate through the pores, we weigh the water obtained from the collectors in a given amount of time and then calculate the volumetric flow rate using water density $\rho = 998.2$ kg/m^3 at a room temperature of 20 °C.

For particle selectivity, we suspend polystyrene particles (Maxi-Blast, PB-2.5) in deionized water at a concentration of 0.2 g/L, where the particles have an average diameter of 324 μm and a SD of 51 μm. Because our particles have a slightly higher density (1,050 kg/m^3) than water, an overhead stirrer (ONiLAB) is employed to mix the solution thoroughly. For visualization (Fig. 4A), we choose an average channel velocity of 0.5 m/s and record the motion of particles using a high-speed camera (Phantom Miro M320S) at 3,400 frames per second. Individual images are then overlaid to show the trajectories of several sizes of particles. Finally, we capture microscopic images (XIMEA xiQ) of the particles obtained from the water collectors and analyze their size distributions using ImageJ2 (NIH).

Numerical Methods. Fluid flow in the leaky channel is simulated using a pressure-based finite-volume solver, where 2D and 3D simulations are realized in Ansys Fluent and OpenFOAM, respectively (see inlet velocity profiles and definitions of boundary conditions in *SI Appendix*, Text B and Fig. S5A, respectively). We employ second-order discretization schemes and choose a relative residual of 10^{-6} for mass and velocity as the stop criterion. Specifically, we add a small section of nonleaking wall near the outlet to avoid numerical instability and to be consistent with the experiments. To ensure mesh independence, we monitor the pressure and the y-velocity component near the inlet and the outlet of pores, respectively, at varying grid resolutions (*SI Appendix*, Figs. S5 B and C).

The pore-scale leaking rate Q_{leak} is obtained by integrating the y-velocity component across a pore, and the average leaking velocity is $q_{leak} = Q_{leak}/T$ in 2D and Q_{leak}/TH in 3D. To calculate particle trajectories in 2D (*SI Appendix*, Fig. S11), we employ the Lagrangian particle tracking module in Ansys Fluent, incorporating Stokes drag, pressure gradient, added mass, and lift force as source terms. Additionally, we introduce a user-defined near-wall lubrication force to prevent particles from intersecting with the walls (*SI Appendix*, Text H).

To compute Q_{leak} and $d_{p,c}$ for the ten mobula species, we convert the mobula filter lobes into equivalent linear filter plates. For this, the geometric data are either collected from the literature (34) or measured from illustrations (30, 33), where the tilting angle θ is assumed to be 0.47 and 0.61, respectively, for manta rays and devil rays (34). The tilting angle is assumed to be 0.47 for the numerically obtained contour lines in Fig. 5B. Unless otherwise mentioned, we choose a half-channel width of 25 mm, which is on the same order of magnitude as the channel size in the mobula cavity. For Fig. 5B, the filter plate thickness scales with l_{pore}/d for $d < 0.2$ mm; otherwise, the filter plate thickness is 0.5 mm throughout our study.

Author affiliations: [a]Department of Mechanical Engineering, Massachusetts Institute of Technology, Cambridge, MA 02139; and [b]Department of Mathematics, Massachusetts Institute of Technology, Cambridge, MA 02139

1. D. B. Purchas, K. Sutherland, *Handbook of Filter Media* (Elsevier Science, Amsterdam, The Netherlands, ed. 2, 2002), pp. 1–34.
2. R. W. Baker, *Membrane Technology and Applications* (John Wiley & Sons, Ltd, ed. 3, 2012).
3. S. Yu, L. Pan, Y. Zhang, X. Chen, X. Hou, Liquid gating technology. *Pure Appl. Chem.* **93**, 1353–1370 (2021).
4. M. A. Alkhadra et al., Electrochemical methods for water purification, ion separations, and energy conversion. *Chem. Rev.* **122**, 13547–13635 (2022).
5. Y. Zhang et al., Continuous air purification by aqueous interface filtration and absorption. *Nature* **610**, 74–80 (2022).
6. D. T. Nguyen, S. Lee, K. P. Lopez, J. Lee, A. P. Straub, Pressure-driven distillation using air-trapping membranes for fast and selective water purification. *Sci. Adv.* **9**, eadg6638 (2023).
7. M. Shirato, T. Murase, E. Iritani, F. M. Tiller, A. F. Alciatore, *Filtration in the Chemical Process Industry in Filtration* (Routledge, New York, NY, 2017), pp. 299–423.
8. S. Li et al., Hydrophobic polyamide nanofilms provide rapid transport for crude oil separation. *Science* **377**, 1555–1561 (2022).
9. F. Lipnizki, "Cross-flow membrane applications in the food industry" in *Membrane Technology: Volume 3: Membranes for Food Applications*, K.-V. Peinemann, S. P. Nunes, L. Giorno, Eds. (Wiley Online Library, 2010), pp. 1–24.
10. C. Charcosset, *Membrane Processes in Biotechnology and Pharmaceutics* (Elsevier, Amsterdam, The Netherlands, 2012), pp. 101–141.
11. M. Y. Jaffrin, Hydrodynamic techniques to enhance membrane filtration. *Annu. Rev. Fluid Mech.* **44**, 77–96 (2012).
12. P. Pal, "Water treatment by membrane-separation technology" in *Industrial Water Treatment Process Technology* (Butterworth-Heinemann, 2017), pp. 173–242.
13. J. A. Goldbogen et al., How baleen whales feed: The biomechanics of engulfment and filtration. *Annu. Rev. Mar. Sci.* **9**, 367–386 (2017).
14. P. J. Motta et al., Feeding anatomy, filter-feeding rate, and diet of whale sharks *Rhincodon typus* during surface ram filter feeding off the Yucatan Peninsula, Mexico. *Zoology* **113**, 199–212 (2010).
15. K. R. Sutherland, L. P. Madin, R. Stocker, Filtration of submicrometer particles by pelagic tunicates. *Proc. Natl. Acad. Sci. U.S.A.* **107**, 15129–15134 (2010).
16. L. T. Nielsen et al., Hydrodynamics of microbial filter feeding. *Proc. Natl. Acad. Sci. U.S.A.* **114**, 9373–9378 (2017).
17. H. U. Riisgård, P. S. Larsen, Particle capture mechanisms in suspension-feeding invertebrates. *Mar. Ecol. Prog. Ser.* **418**, 255–293 (2010).

18. K. R. Conley, F. Lombard, K. R. Sutherland, Mammoth grazers on the ocean's minuteness: A review of selective feeding using mucous meshes. *Proc. R. Soc. B: Biol. Sci.* **285**, 20180056 (2018).

19. L. Hamann, A. Blanke, Suspension feeders: Diversity, principles of particle separation and biomimetic potential. *J. R. Soc. Interface* **19**, 20210741 (2022).

20. S. L. Sanderson, E. Roberts, J. Lineburg, H. Brooks, Fish mouths as engineering structures for vortical cross-step filtration. *Nat. Commun.* **7**, 11092 (2016).

21. G. Falcucci *et al.*, Extreme flow simulations reveal skeletal adaptations of deep-sea sponges. *Nature* **595**, 537–541 (2021).

22. A. L. Rypstra, Building a better insect trap: An experimental investigation of prey capture in a variety of spider webs. *Oecologia* **52**, 31–36 (1982).

23. G. Zweers, F. de Jong, H. Berkhoudt, J. C. V. Berge, Filter feeding in flamingos (*Phoenicopterus ruber*). *Condor* **97**, 297–324 (1995).

24. M. Jaffar-Bandjee, T. Steinmann, G. Krijnen, J. Casas, Insect pectinate antennae maximize odor capture efficiency at intermediate flight speeds. *Proc. Natl. Acad. Sci. U.S.A.* **117**, 28126–28133 (2020).

25. T. L. Spencer *et al.*, Moth-inspired methods for particle capture on a cylinder. *J. Fluid Mech.* **884**, A34 (2020).

26. H. G. Andrews, E. A. Eccles, W. C. E. Schofield, J. P. S. Badyal, Three-dimensional hierarchical structures for fog harvesting. *Langmuir* **27**, 3798–3802 (2011).

27. K. Ramchander *et al.*, Engineering and characterization of gymnosperm sapwood toward enabling the design of water filtration devices. *Nat. Commun.* **12**, 1871 (2021).

28. D. I. Rubenstein, M. A. R. Koehl, The mechanisms of filter feeding: Some theoretical considerations. *Am. Nat.* **111**, 981–994 (1977).

29. S. L. Sanderson, A. Y. Cheer, J. S. Goodrich, J. D. Graziano, W. T. Callan, Crossflow filtration in suspension-feeding fishes. *Nature* **412**, 439–441 (2001).

30. G. Stevens, D. Fernando, M. Dando, G. Notarbartolo-Di-Sciara, *Guide to the Manta and Devil Rays of the World* (Princeton University Press, 2018).

31. G. Notarbartolo-Di-Sciara, A revisionary study of the genus Mobula Rafinesque, 1810 (Chondrichthyes: Mobulidae) with the description of a new species. *Zool. J. Linnean Soc.* **91**, 1–91 (1987).

32. E. W. M. Paig-Tran, T. Kleinteich, A. P. Summers, The filter pads and filtration mechanisms of the devil rays: Variation at macro and microscopic scales. *J. Morphol.* **274**, 1026–1043 (2013).

33. E. W. M. Paig-Tran, A. P. Summers, Comparison of the structure and composition of the branchial filters in suspension feeding elasmobranchs. *Anat. Rec.* **297**, 701–715 (2014).

34. R. V. Divi, J. A. Strother, E. W. M. Paig-Tran, Manta rays feed using ricochet separation, a novel nonclogging filtration mechanism. *Sci. Adv.* **4**, eaat9533 (2018).

35. M. M. Pendergast, R. Mika Dorin, W. A. Phillip, U. Wiesner, E. M. Hoek, Understanding the structure and performance of self-assembled triblock terpolymer membranes. *J. Membr. Sci.* **444**, 461–468 (2013).

36. X. Qiu *et al.*, Selective separation of similarly sized proteins with tunable nanoporous block copolymer membranes. *ACS Nano* **7**, 768–776 (2013).

37. J. R. Werber, C. O. Osuji, M. Elimelech, Materials for next-generation desalination and water purification membranes. *Nat. Rev. Mater.* **1**, 16018 (2016).

38. A. S. Berman, Laminar flow in channels with porous walls. *J. Appl. Phys.* **24**, 1232–1235 (1953).

39. M. Kostoglou, A. J. Karabelas, Comprehensive simulation of flat-sheet membrane element performance in steady state desalination. *Desalination* **316**, 91–102 (2013).

40. A. Mehta, A. L. Zydney, Permeability and selectivity analysis for ultrafiltration membranes. *J. Membr. Sci.* **249**, 245–249 (2005).

41. H. B. Park, J. Kamcev, L. M. Robeson, M. Elimelech, B. D. Freeman, Maximizing the right stuff: The trade-off between membrane permeability and selectivity. *Science* **356**, eaab0530 (2017).

42. R. M. Dorin *et al.*, Designing block copolymer architectures for targeted membrane performance. *Polymer* **55**, 347–353 (2014).

43. S. K. Karode, Laminar flow in channels with porous walls, revisited. *J. Membr. Sci.* **191**, 237–241 (2001).

44. M. Kim, A. L. Zydney, Theoretical analysis of particle trajectories and sieving in a two-dimensional cross-flow filtration system. *J. Membr. Sci.* **281**, 666–675 (2006).

45. A. B. Haque *et al.*, Fishing and trade of devil rays (*Mobula* spp.) in the Bay of Bengal, Bangladesh: Insights from fishers' knowledge. *Aquat. Conserv.: Mar. Freshwater Ecosyst.* **31**, 1392–1409 (2021).

46. K. Hiemenz, Die Grenzschicht an einem in den gleichförmigen Flüssigkeitsstrom eingetauchten geraden Kreiszylinder. *Dinglers Polytech. J.* **326**, 321–324 (1911).

47. D. W. Inglis, J. A. Davis, R. H. Austin, J. C. Sturm, Critical particle size for fractionation by deterministic lateral displacement. *Lab Chip* **6**, 655–658 (2006).

48. E. M. Witkop, S. V. Wassenbergh, P. D. Heideman, S. L. Sanderson, Biomimetic models of fish gill rakers as lateral displacement arrays for particle separation. *Bioinsp. Biomimetics* **18**, 056009 (2023).

49. M. R. Maxey, J. J. Riley, Equation of motion for a small rigid sphere in a nonuniform flow. *Phys. Fluids* **26**, 883–889 (1983).

50. D. Vigolo, I. M. Griffiths, S. Radl, H. A. Stone, An experimental and theoretical investigation of particle-wall impacts in a T-junction. *J. Fluid Mech.* **727**, 236–255 (2013).

51. M. Garcia, B. Ganapathysubramanian, S. Pennathur, A linearised model for calculating inertial forces on a particle in the presence of a permeate flow. *J. Fluid Mech.* **861**, 253–274 (2019).

52. D. L. Chase, C. Kurzthaler, H. A. Stone, Hydrodynamically induced helical particle drift due to patterned surfaces. *Proc. Natl. Acad. Sci. U.S.A.* **119**, e2202082119 (2022).

53. X. Mao, I. Bischofberger, A. E. Hosoi, Particle focusing in a wavy channel. *J. Fluid Mech.* **968**, A25 (2023).

54. E. W. M. Paig-Tran, J. J. Bizzarro, J. A. Strother, A. P. Summers, Bottles as models: Predicting the effects of varying swimming speed and morphology on size selectivity and filtering efficiency in fishes. *J. Exp. Biol.* **214**, 1643–1654 (2011).